ROYAL SOCIETY OF CHEMISTRY

PAPER

Check for updates

Modulating heterointerfaces of tungsten incorporated CoSe/Co₃O₄ as a highly efficient electrocatalyst for overall water splitting†

Ravichandran Balaji, [ID] [a] Thanh Tuan Nguyen, [ID] [a] Kempanna Harish, [ID] [a] Nam Hoon Kim [ID] *[a] and Joong Hee Lee [ID] *[ab]

Electrochemical water-splitting is emerging as a promising pathway to produce pure and green hydrogen. However, the sluggish kinetics of the oxygen evolution reaction (OER) and slow reaction rate of the hydrogen evolution reaction (HER) remain challenging issues. The state-of-the-art Pt and RuO₂/IrO₂ electrocatalysts demonstrate excellent HER and OER performance. However, the scarcity and high cost hinder their practical applications. Herein, we present a novel approach to design a WCoSe/WCo₃O₄ heterostructure and use it as an effective bifunctional electrocatalyst for overall water-splitting. The synergistic effect of W and Co metal cations in the heterogeneous phase of Se and O anions could increase the charge transfer and electronic modulation of the material which could improve the catalytic activities. The water electrolysis device with the WCoSe/WCo₃O₄ heterostructure as a bifunctional catalyst required a small cell voltage of ~1.49 and 1.66 V at current densities of 10 and 100 mA cm^{-2}. Furthermore, the water-splitting cell displayed an exceptional durability of 100 h, surpassing the state-of-the-art Pt/C‖RuO₂ electrolyzer. This work offers a promising approach to construct novel 3D heterostructure electrocatalysts, which would be suitable for various energy conversion applications.

Introduction

The global demand for renewable and clean energy sources has exclusively increased due to the enormous consumption of fossil fuels and environmental impact.[1–4] Hydrogen is known to be one of the best alternative fuels because of its high energy density and sustainability. However, conventional hydrogen production is still carried out from natural gas, which releases carbon during the process. Recently, electrochemical water splitting has been demonstrated as an efficient strategy to separate the water molecules into hydrogen and oxygen with zero-carbon emission.[5] In general, water splitting includes two half-reactions, namely the hydrogen evolution reaction (HER) and the oxygen evolution reaction (OER), which require a high overpotential and present sluggish kinetics.[3,6] To overcome these issues, much effort has been made to develop a highly active electrochemical catalyst and reduce the overpotential.[7–9] Traditionally, noble metal-based materials such as Pt, RuO₂,

and IrO₂ were displayed as highly active catalysts for the HER and OER, which could efficiently enhance the dynamic kinetics and reduce the overpotential.[10–13] However, their scarcity and high installation cost limit their large-scale requirement for industrial applications. Moreover, almost all present electrocatalysts exhibit a single functional activity due to their incompatibility in different electrolytes, increasing the fabrication cost and releasing contaminants.[14,15] Therefore, the development of earth-abundant bifunctional catalysts with enhanced electrochemical performance and cost-effectiveness would represent a significant innovation for water electrolyzers.

Transition metal compounds (TMCs) have been explored as promising electrocatalysts, owing to their advantageous intrinsic structure, excellent electrochemical activities, and low cost.[4,16,17] Among them, metal oxides have been exhibited as promising electrocatalysts for the alkaline electrolyzer, due to their high catalytic activities with a small overpotential and excellent faradaic efficiency.[18–20] However, due to the insufficient electrical conductivity of metal oxide which inhibits the electron transport and reduces electrochemical performance of the catalysts.[21,22] Recently, metal selenide-based catalysts have been preferred for bifunctional activities owing to their higher electrical conductivity, numerous active sites, and intrinsic electrocatalytic capability compared to metal oxides.[23–25] Notably, to achieve better electrocatalytic performance, different strategies such as tuning electronic structures, defect enrichments, and heterostructure interfaces have been

[a]Advanced Materials Institute of Nano Convergence Engineering (BK21 FOUR), Dept. of Nano Convergence Engineering, Jeonbuk National University, Jeonju, Jeonbuk 54896, Republic of Korea. E-mail: jhl@jbnu.ac.kr; nhk@jbnu.ac.kr; Tel: +82 63 270 2342. Fax: +82 63 270 2301

[b]Carbon Composite Research Centre, Department of Polymer-Nano Science and Technology, Jeonbuk National University, Jeonju, Jeonbuk 54896, Republic of Korea

† Electronic supplementary information (ESI) available. See DOI: 10.1039/d1ta09932a

employed by controlling the synthesis protocol of the electrocatalyst.[10,26–28] Among them, heterostructure materials have proven excellent theoretical and experimental outcomes and are dominated by their interfacial activity and electronic structure.[29–32] Also, inspired by their atomic arrangements and electronic structure, different nanostructures can be effective for boosting electrocatalytic performance of materials. Moreover, incorporating selenide as a secondary species extensively increases the electrocatalytic performance.

Currently, H_2 adsorption is established as a functional aspect to estimate the intrinsic HER activity of the electrocatalyst, where the optimal onset overpotential value for the HER is close to zero under neutral and alkaline conditions.[33,34] In addition, alkali water reduction was hindered by slow water dissociation which makes it difficult to evaluate the efficiency of the electrocatalytic activity (*i.e.*, $H_2O + e^- \rightarrow OH^- + H_{ad}$). Researchers have devoted great effort to design effective electrocatalysts for promoting the active sites and Volmer step reaction in alkali water splitting using H^+ (proton) on the surface of the catalyst.[8,34–37] For example, Zhang and co-workers presented the *in situ* surface reconstruction of a TiO_2@CoCH composite which accelerates the HER kinetics by activating the surface and boosting the electrochemical performance in alkali media.[34] Liu *et al.* established a multiphase $CoNiP/Co_xP$ heterostructure with unique kinetics helpful to enhance the water dissociation at the heterointerface and boost the hydrogen production.[34] Zhang *et al.* synthesized the $NiFe_2O_4/FeNi_2S_4$ heterostructure where the oxide/sulfide heterojunction was formed with enriched oxygenated species, it could accelerate the kinetics of catalyst.[8] Luo *et al.* proposed that $Mo–Ni_3S_2/Ni_xP_y$ hollow nanorod heterostructures were obtained by partial phosphorization and the controlled doping of Mo, which could assist in tuning their electronic structure. $Mo–Ni_3S_2/Ni_xP_y$ possesses a strong coupling effect which exhibits high catalytic kinetics and excellent rate stability.[37] Zheng *et al.* demonstrated that the atomic interface engineering of $NiSe_2/CoSe_2$ could effectively regulate the electron transfer of bimetallic sites in the heterostructure catalyst and optimal binding energy with oxygenated species and accelerate the redox kinetics by enhancing the synergistic effect between selenides and surface oxides/hydroxides.[37] In addition, the adsorption of hydrogen atoms on the surface of the catalyst plays an important role in generating molecular H_2.[38–40] Therefore, the exposure of atomic and electronic interface configurations at low voltage polarization is required. Considering the beneficial behavior, it is essential to develop rational heterostructures through the combined regulation of architectural morphology and heterostructures, and engineering active sites, to enhance bifunctional kinetics towards large-scale electrolysis.

Herein, a novel strategy to design a 3D hierarchical $WCoSe/WCo_3O_4$ heterostructure were presented with controllable atomic surface configurations involving interface engineering through effective selenization and the partial oxidation process. The effective formation of the $WCoSe/WCo_3O_4$ heterostructure was investigated, which could fine-tune the electronic nanostructures and maximize the active catalyst sites. The abundant heterointerfaces with an enriched oxygen phase were well

controlled, which could significantly reduce the overpotential and improve the stability for OER performance. Moreover, $WCoSe/WCo_3O_4$ increases the hydrogen atom adsorption and boosts the H_2 molecule generation during the HER process. Remarkably, the electrolyzer with the $WCoSe/WCo_3O_4$ heterostructure bifunctional catalyst for both the anode and cathode required a small cell voltage of ~1.49 V and 1.66 V at different current densities of 10 and 100 mA cm^{-2}, respectively. The water-splitting cell exhibited an outstanding durability of 100 h, which surpassed that of the Pt/C∥RuO$_2$ electrolyzer. This work demonstrates a promising approach to fabricate robust heterostructures at low-cost and with excellent bifunctional electrocatalytic activity, which could be promising alternative electrocatalysts for industrial applications.

Experimental

Synthesis of the WCo precursor

All chemicals and reagents were purchased from Sigma-Aldrich (Merck) and were used directly without any purification. First, 1 mmol sodium metatungstate hydrate ($Na_6W_{12}O_{39} \cdot H_2O$) and 1 mmol cobalt nitrate hexahydrate ($Co(NO_3)_2 \cdot 6H_2O$) were dissolved in 50 mL of DI water, and stirred for 15 min. Then, the reaction solution was transferred to an 80 mL Teflon autoclave with a cleaned Ni-foam substrate (5 cm × 2 cm). After that, the reaction was carried out at ~160 °C for 16 h. Subsequently, the resulting product WCo precursor was collected, rinsed with DI water and ethanol several times, and dried overnight at ~60 °C in a vacuum oven.

Synthesis of the 3D hierarchical $WCoSe/WCo_3O_4$ heterostructure

The as-obtained WCo precursor was immersed in 50 mL DI water containing selenium powder (Se) and $NaBH_4$ (molar ratio 1 : 2). The prepared mixture was transferred to a Teflon autoclave for further selenization at ~180 °C for 4 h. After that, the as-obtained material was rinsed in DI water and ethanol, and then vacuum dried at ~60 °C. Next, WCoSe was subjected to partial oxidation treatment by calcining in an air atmosphere at 300 °C for 2 h to form the free-standing $WCoSe/WCo_3O_4$ heterostructure. The mass loading of $WCoSe/WCo_3O_4$ (~3.02 mg cm^{-2}) was measured with a balance for 3 samples and the average value was taken. For comparison, we used a similar procedure to synthesize the heterostructures of single metal $CoSe/Co_3O_4$ and WSe_2/WO_2.

Characterization techniques

The as-synthesized electrocatalysts were examined by scanning electron microscopy (SEM; SUPRA 40 VP; Carl Zeiss, Germany) at the Center for University-wide Research Facilities (CURF) of Jeonbuk National University, Jeonju, South Korea. Transmission electron microscopy (TEM; JEM-ARM200F, Japan), high-resolution TEM (HR-TEM), and fast Fourier transform (FFT) were performed at Korea Basic Science Institute (KBSI), Jeonju Centre, JBNU, South Korea; energy-dispersive X-ray spectroscopy (EDAX; SUPRA 40 VP; Carl Zeiss, Germany) was

This journal is © The Royal Society of Chemistry 2022

J. Mater. Chem. A, 2022, **10**, 3782–3792 | **3783**

also conducted. The crystallinity of the electrocatalysts was analyzed by X-ray diffraction (XRD; Cu Kα radiation, $\lambda = 0.154$ nm) at CURF. The BET surface area and pore size distribution were characterized by using a Micromeritics ASAP 2020. Note that the BET surface area was taken on the powder form of the material. X-ray photoelectron spectroscopy (XPS) measurements were performed using a NEXSA (Thermo Fisher Scientific, UK) in KBSI, Jeonju Center.

Electrochemical measurements

The electrochemical performance of the as-prepared catalysts was tested on a CHI 760E (CH Instruments Inc., USA) electrochemical workstation at room temperature. In the three-electrode system, the heterostructure electrocatalyst was used directly as a working electrode, while the graphite rod and Hg/HgO were employed as counter and reference electrodes, respectively. Linear sweep voltammetry (LSV) was performed in 1.0 M KOH solution at a scan rate of 1 mV s^{-1}. The stability of the catalysts was measured by chronopotentiometry at current densities of 10 and 100 mA cm^{-2}. Electrochemical impedance

spectroscopy (EIS) was carried out with different frequencies from 0.1 to 10^6 Hz. The electrochemical active surface area (ECSA) of the catalysts was assessed by cyclic voltammetry (CV) in a non-faradaic potential region of (0.86–0.98 V) at different scan rates to achieve the double-layer capacitance (C_{dl}) value of the catalysts, which could be derived from the following equation.[41]

$$\text{ECSA} = \frac{C_{dl}}{C_S} \tag{1}$$

The C_{dl} value calculated from half of the slope of the curve is consistent with the reactive surface area of the materials. The difference between the anodic current density (J_a) and the cathodic current density (J_c) at a given potential value was calculated using the following equation.

$$\Delta j = \frac{(j_a - j_b)}{2} \tag{2}$$

A plotted line based on ΔJ vs. the scan rate was built and then fitted to a linear regression curve.

Scheme 1 Design and fabrication of the WCoSe/WCo$_3$O$_4$ heterostructure *via* controlled surface atomic configuration for the alkaline medium electrochemical water–electrolyzer.

3784 | *J. Mater. Chem. A*, 2022, **10**, 3782–3792

This journal is © The Royal Society of Chemistry 2022

Results and discussion

Morphological investigation of the WCoSe/WCo$_3$O$_4$ heterostructure

The schematic representation of the fabrication of the 3D hierarchical WCoSe/WCo$_3$O$_4$ heterostructure is shown in Scheme 1. The WCo precursor was first selenized, followed by controlled partial oxidation with an induced surface modification strategy. Finally, the as-prepared electrodes were used directly as bifunctional catalysts for water splitting applications. We used field emission scanning electron microscopy (FE-SEM) to investigate the topological structure of the WCoSe/WCo$_3$O$_4$ heterostructure (Fig. 1a, b, and S1†). First, the WCo precursor was successfully observed and exhibited plentiful nanosheets growing on nickel foam that could provide a high surface area (Fig. S1†). After that, the WCo precursor was subsequently selenized, followed by a partial oxidation process to convert WCoSe into the WCoSe/WCo$_3$O$_4$ heterostructure. The EDS-SEM color mapping further confirmed the uniform contribution of the W, Co, O, and Se elements (Fig. 1e) in the WCoSe/WCo$_3$O$_4$ heterostructure. In contrast, pure WSe$_2$/WO$_2$ displayed a closely packed nanosheet morphology that randomly grew on the nickel foam substrate and might collapse during the stability test. At the same time, the CoSe/Co$_3$O$_4$ counterpart presented a nanorod configuration, which could reduce the active sites, thereby decreasing the electrochemical performance.

To further validate the architectures of the 3D hierarchical WCoSe/WCo$_3$O$_4$ heterostructure, we have accomplished transmission electron microscopy (TEM) and high-resolution TEM (HR-TEM), and the results are illustrated in Fig. 2a and d. The TEM image shows a sheet-like structure of WCoSe/WCo$_3$O$_4$ with numerous nanopores (Fig. 2a). The selected area diffraction (SAED) pattern in Fig. 2b showed the polycrystalline nature of the WCoSe/WCo$_3$O$_4$ heterostructure. The HR-TEM image of the WCoSe/WCo$_3$O$_4$ heterostructure clearly shows lattice fringes of ~0.191 nm for the (105) plane of WSe$_2$ and ~0.169 nm for the (232) plane of WO$_2$ (ICDD #00-048-1827), respectively (Fig. 2c). Similarly, the typical lattice fringes of ~0.226, 0.248 and 0.158 nm could be assigned to the (111), (311), and (511) planes of CoSe and Co$_3$O$_4$, respectively (Fig. 2c). In addition, the HR-TEM image of the WCoSe/WCo$_3$O$_4$ heterostructure clearly exhibits the heterointerfaces between different crystals of Co$_3$O$_4$ and CoSe. Fig. 2d shows the fast Fourier transform (FFT) spectra validating the high crystalline structure of the as-prepared WCoSe/WCo$_3$O$_4$ heterostructure. Furthermore, high-angle annular dark-field scanning transmission electron microscopy (HAADF-STEM) analysis was used to examine the distribution of tungsten, cobalt, oxygen, and selenide elements in the WCoSe/

Fig. 1 FE–SEM images of (a) WSe$_2$/WO$_2$ and (b) CoSe/Co$_3$O$_4$, (c) low and (d) high magnification images of the WCoSe/WCo$_3$O$_4$ heterostructure, and (e) EDS color mapping with the corresponding elements of W, Co, O, and Se of the WCoSe/WCo$_3$O$_4$ heterostructure.

This journal is © The Royal Society of Chemistry 2022

J. Mater. Chem. A, 2022, **10**, 3782–3792 | **3785**

Fig. 2 Intrinsic morphology of the WCoSe/WCo$_3$O$_4$ heterostructure. (a) TEM, (b) corresponding SAED, (c) HR-TEM, (d) FFT, and (e) STEM and STEM-EDS color mapping with the distribution of Co, W, O, and Se elements.

WCo$_3$O$_4$ heterostructure (Fig. 2e). This study clearly reveals negligible elemental segregation and the successful partial oxidation of WCoSe to form the WCoSe/WCo$_3$O$_4$ heterostructure. The nanointerfaces at the atomic level and the slight lattice distortions are expected to afford more active sites with high catalytic activity for binding with oxygen-containing intermediates. The partial formation of oxygen species and incorporation of hydrogen of the WCoSe/WCo$_3$O$_4$ heterostructure could enhance the durability and provide more electroactive sites of electrocatalysts during OER and HER.

X-ray diffraction (XRD) was used to examine the phase purity and crystal structure of the WCoSe/WCo$_3$O$_4$ heterostructure, CoSe/Co$_3$O$_4$, and WSe$_2$/WO$_2$ (Fig. 3a). The XRD patterns of CoSe/Co$_3$O$_4$ exhibited typical peaks at $2\theta \sim$36.3, 58.4, and 64.2° which are assigned to the (311), (511), and (440) planes of Co$_3$O$_4$ (ICDD #01-080-1540) and $\sim$30.4, 39.9, and 50.4° corresponding to the (101), (111) and (112) planes of CoSe (ICDD #01-077-8900). Besides, WSe$_2$/WO$_2$ showed peaks positioned at $2\theta \sim$37.8, 47.4, and 55.9 and 23.2, 36.9, and 53.8° which are attributed to the (103), (105) and (110) planes of WSe$_2$ (ICDD #01-071-0600) as well as the (111), (230), and (232) planes of WO$_2$ (ICDD #00-048-1827).[42,43] Moreover, the XRD patterns of the WCoSe/WCo$_3$O$_4$ heterostructure exhibited prominent diffraction peaks at 2θ

$\sim$23.2, 36.3, 53.8, 58.4 and 64.2° corresponding to the (111), (311), (511), (110), and (440) planes of the WCoO$_x$ nanohybrids,[38] whereas the strong peaks that are observed at 30.4, 47.4, and 55.9° are assigned to the (101), (105), and (110) planes of WCoSe$_x$.[44] This further confirms the successful partial oxidation of WCoSe nanosheets to corresponding CoO$_x$ to form the WCoSe/WCo$_3$O$_4$ heterostructure, which is well-consistent with TEM analysis. The partial oxidation of WCoSe could result in the slight shifting of the peaks towards higher 2θ (Fig. S2†).[45] The valence states, surface electronic structures, and chemical compositions of the WCoSe/WCo$_3$O$_4$(I), WSe$_2$/WO$_2$(II), and CoSe/Co$_3$O$_4$(III) heterostructures were demonstrated by X-ray photoelectron spectroscopy (XPS), as shown in Fig. 3b–e. The survey XPS spectrum indicates the existence of W, Co, O, and Se elements in the WCoSe/WCo$_3$O$_4$ heterostructure (Fig. S3†). As illustrated in Fig. 3b, the deconvolution of W 4f spectra exhibited four typical peaks at $\sim$34.3–34.6 and 36.5–36.7, corresponding to W 4f$_{7/2}$ and W 4f$_{5/2}$, respectively.[46,47] The W 4f peak for WCoSe/WCo$_3$O$_4$ shifted to a higher binding energy due to coupling interaction between the heterostructures. In addition, the peaks positioned at the binding energies of $\sim$38.7–40.1 and 40.8–41.1 eV indicated W^{6+} from surface oxidation, which proves the presence of W in the WCoSe/WCo$_3$O$_4$

3786 | J. Mater. Chem. A, 2022, **10**, 3782–3792

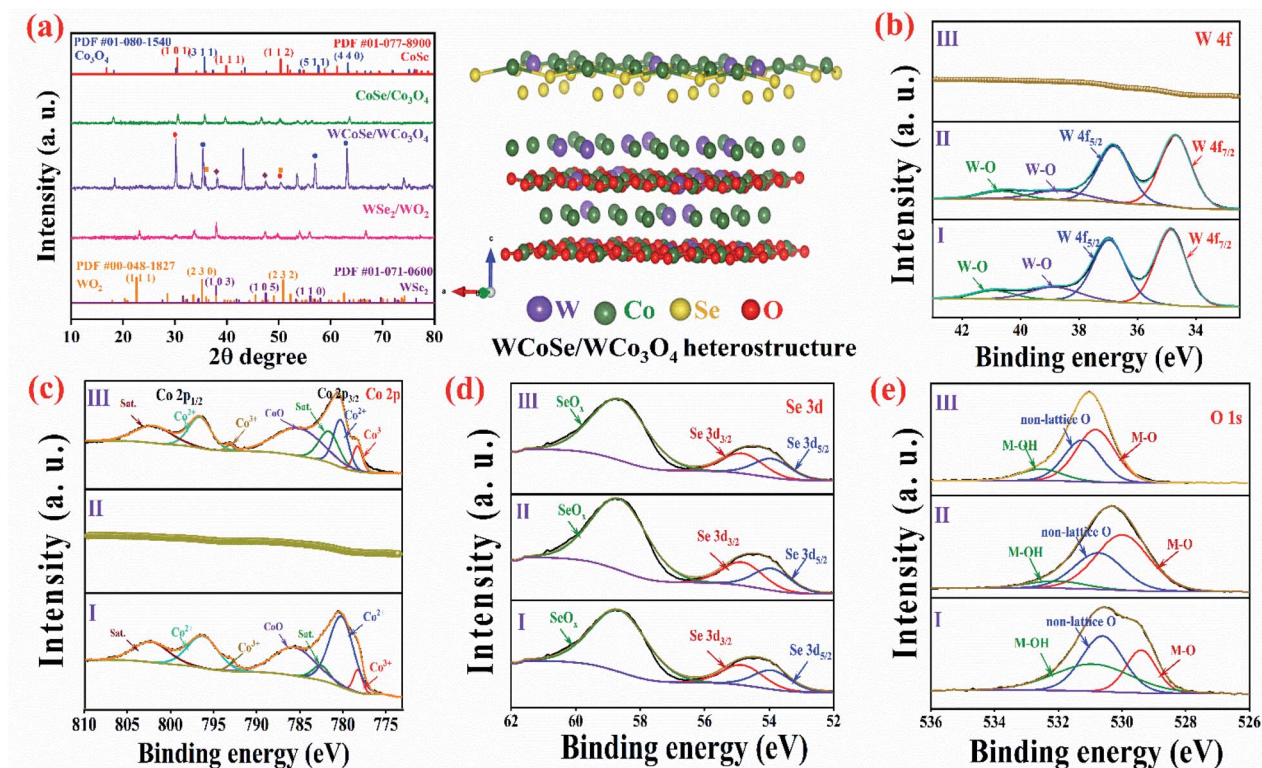This journal is © The Royal Society of Chemistry 2022

Fig. 3 (a) XRD patterns for the as-synthesized materials and structural alignments of the WCoSe/WCo$_3$O$_4$ heterostructure. XPS spectra of (b) W 4f, (c) Co 2p, (d) Se 3d, and (e) O 1s present in the WCoSe/WCo$_3$O$_4$ heterostructure.

heterostructure.[46,47] Moreover, the high-resolution Co 2p spectrum could be deconvoluted into Co 2p$_{1/2}$ ($\sim$797.1–797.4 and 793.1–793.4 eV) and Co 2p$_{3/2}$ ($\sim$780.1–780.3 and 778.2–778.8 eV) which demonstrated the presence of Co^{2+} and Co^{3+} species in the heterostructure. The peak position of Co in the WCoSe/WCo$_3$O$_4$ heterostructure tends to move to a lower binding energy, illustrating the electron deficient state of Co sites.[48–50] The deconvoluted Se 3d spectrum exhibits three peaks at $\sim$53.8–54.1, 55.1–55.4, and 58.7–59.2 eV, corresponding to 3d$_{5/2}$, 3d$_{3/2}$, and SeO$_x$, respectively (Fig. 3d).[51] Moreover, Fig. 3e shows the multiple oxygen states of O 1s spectra that indicate the WCoSe/WCo$_3$O$_4$ heterostructure. The oxygen peaks observed at a binding energy of $\sim$529.2 and 532.8 eV correspond to the metal–O bond, non-lattice O, and M–OH, respectively. These results display the strong electronic coupling interaction between various elements in the WCoSe/WCo$_3$O$_4$ heterostructure, proving that the optimal nanostructure could play a key role in boosting the electrochemical performance.

Electrocatalytic performance of the WCoSe/WCo$_3$O$_4$ heterostructure

Based on the nanostructure characterization, we further analyzed the oxygen evolution reaction (OER) performance of the WCoSe/WCo$_3$O$_4$ heterostructure and WSe$_2$/WO$_2$ and CoSe/Co$_3$O$_4$ nanohybrids in 1 M KOH alkaline electrolyte using a three-electrode configuration.

The mechanism reaction process for OER in alkaline electrolyte follows these equations, where M represents the as-synthesized electrocatalyst.

$$M + OH^- \rightarrow M–OH + e^-$$

$$M–OH + OH^- \rightarrow M–O + H_2O + e^-$$

$$M–O + OH^- \rightarrow M–OOH + e^-$$

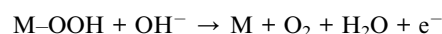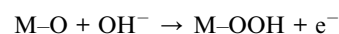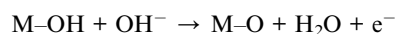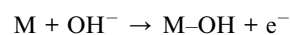$$M–OOH + OH^- \rightarrow M + O_2 + H_2O + e^-$$

Fig. 4a shows the linear sweep voltammetry (LSV) polarization curves of all the as-obtained catalysts at a scan rate of 2 mV s^{-1}. The WCoSe/WCo$_3$O$_4$ heterostructure catalyst exhibits excellent OER performance with a lower overpotential of $\sim$175 mV at a current density of 10 mA cm^{-2}. In contrast, a higher overpotential is required for the corresponding precursor of pure Co LDH ($\sim$258 mV), WCo LDH ($\sim$235 mV), and pure W LDH ($\sim$264 mV), respectively (Fig. S4a†). In addition, the differently controlled heterostructure also required a higher overpotential compared to our WCoSe/WCo$_3$O$_4$ heterostructure catalysts such as WSe$_2$/WO$_2$ ($\sim$260 mV), CoSe/Co$_3$O$_4$ ($\sim$198 mV), and even commercial RuO$_2$ ($\sim$231 mV). Fig. 4c shows the comparative overpotential of WSe$_2$/WO$_2$, WCoSe/WCo$_3$O$_4$, CoSe/Co$_3$O$_4$, and commercial RuO$_2$ catalysts for current densities of 10 and 100 mA cm^{-2}. This further confirms that the
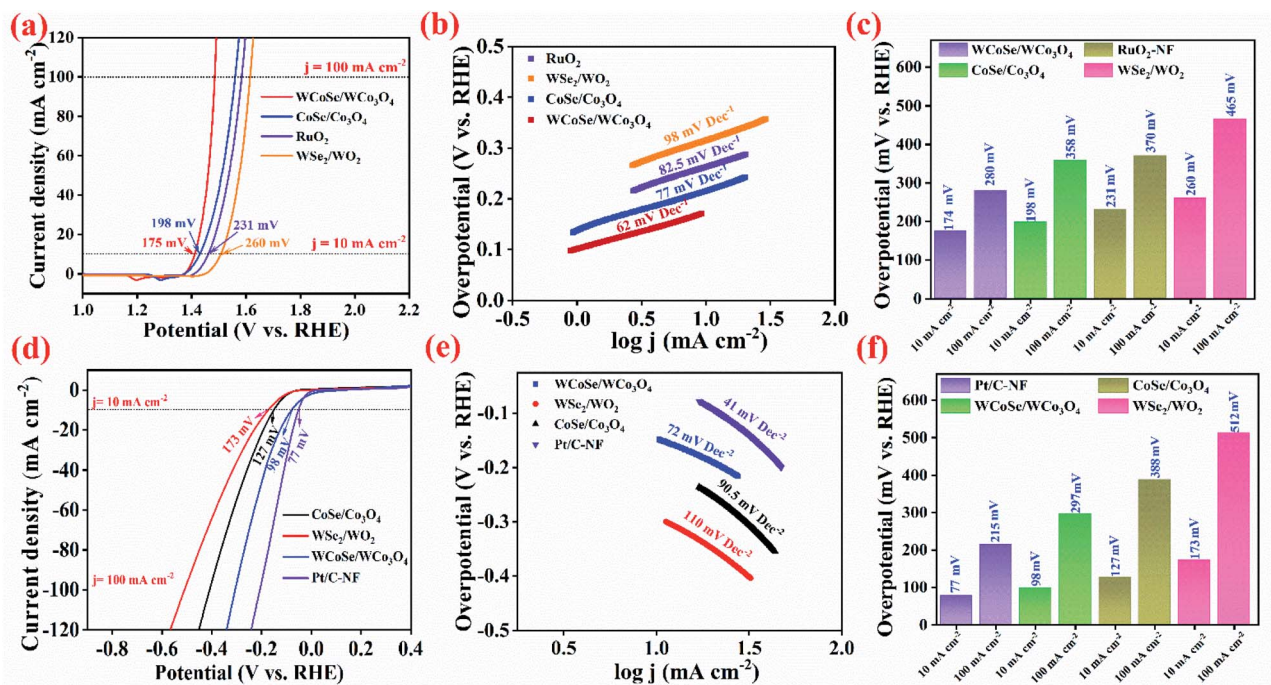
Fig. 4 Electrocatalytic performance of the as-synthesized catalysts for bifunctional activities: (a) LSV polarization curves of WCoSe/WCo$_3$O$_4$ and other comparative electrocatalysts at the scan rate of 2 mV s^{-1} in a 1.0 M KOH alkaline medium and (b) Tafel slopes of WCoSe/WCo$_3$O$_4$ and all other comparative electrocatalysts for the OER performance. (c) Bar graph for overpotential comparison of the as-synthesized electrocatalysts at the current densities of 10 and 100 mA cm^{-2}, (d) LSV polarization curves of WCoSe/WCo$_3$O$_4$ and other comparative electrocatalysts at the scan rate of 2 mV s^{-1} in a 1.0 M KOH alkaline medium and (e) Tafel slopes of WCoSe/WCo$_3$O$_4$ and all other comparative electrocatalysts for the HER performance. (f) Bar graph overpotential comparison of the as-synthesized electrocatalysts at the current densities of 10 and 100 mA cm^{-2}.

WCoSe/WCo$_3$O$_4$ catalyst was superior to other counterparts and most recently reported OER catalysts (Table S1†). To further evaluate the efficiency of the as-synthesized catalysts during the OER process, we have calculated the Tafel slope, and the results are shown in Fig. 4b. The Tafel slope of the WCoSe/WCo$_3$O$_4$ heterostructure based catalyst exhibits the lowest value of 62 mV dec^{-1}, which is superior to that of the corresponding precursor (Fig. S4b†) and other controlled materials of RuO$_2$ (82.5mV dec^{-1}), CoSe/Co$_3$O$_4$ (77 mV dec^{-1}), and WSe$_2$/WO$_2$ (98 mV dec^{-1}), further demonstrating that the WCoSe/WCo$_3$O$_4$ catalyst is favorable for excellent OER kinetics (Fig. 4b). To evaluate the electron transport kinetics and the interface reaction between the electrode/electrolyte during the OER (Fig. S5†), the electrochemical impedance spectra (EIS) were analyzed in the frequency range of 10^6 to 0.1 Hz. The EIS and corresponding fitting curves of all catalysts show that the WCoSe/WCo$_3$O$_4$ catalyst has the smallest charge-transfer resistance (R_{ct}) value of ~0.77 Ω, which is better than that of CoSe/Co$_3$O$_4$ (0.78 Ω) and WSe$_2$/WO$_2$ (1.2 Ω), respectively. These results demonstrate that the optimal heterostructures could enhance the internal electron transport and boost the catalytic performance. Moreover, the solution resistance (R_s) of WCoSe/WCo$_3$O$_4$ is as low as 0.62 Ω, which is smaller than that of CoSe/Co$_3$O$_4$ (0.59 Ω) and WSe$_2$/WO$_2$ (0.97 Ω), indicating the enhanced electron transfer at interfaces of the WCoSe/WCo$_3$O$_4$ heterostructure. Such excellent conductivity can minimize the IR losses and facilitate the charge transfer process in the catalyst electrode. The higher

electron transport contributes to the enhanced OER activities. The electrochemically active surface area (ECSA) represents the interface area between the catalysts and electrolyte, which indicates the utilization and degradation of the catalysts. The ECSA of the electrocatalyst towards the OER could be derived by evaluating the double-layer capacitance (C_{dl}) that could be obtained from the non-redox region of the CV curve (Fig. S6†). The WCoSe/WCo$_3$O$_4$ heterostructure based catalyst shows a high C_{dl} value of 40.52 mF cm^{-2}, (Fig. S7†) compared to that of the other catalysts such as CoSe/Co$_3$O$_4$ (29.81 mF cm^{-2}), WSe$_2$/WO$_2$ (23.83 mF cm^{-2}), and RuO$_2$ (33.09 mF cm^{-2}), respectively, indicating the large number of electroactive sites in the WCoSe/WCo$_3$O$_4$ heterostructure electrocatalyst.

The chronopotentiometric durability test was performed to further prove the practical applicability of the WCoSe/WCo$_3$O$_4$ heterostructure catalyst. Fig. S8a† shows a negligible degradation of the potential after 50 h. In addition, the LSV curves before and after the stability test exhibit the good retention of the WCoSe/WCo$_3$O$_4$ heterostructure electrocatalyst toward the OER (Fig. S8b†). The Nyquist plot of the WCoSe/WCo$_3$O$_4$ catalyst after the long-term electrochemical stability test shows a slightly increased R_{ct} value of ~0.68 Ω, further proving its excellent OER durability. Furthermore, the morphological analysis after the stability test indicates that the retained WCoSe/WCo$_3$O$_4$ electrocatalyst structure without any loss validates its outstanding electrochemical stability towards OER (Fig. S9†). These excellent results for the OER indicated that the

3788 | J. Mater. Chem. A, 2022, 10, 3782–3792

This journal is © The Royal Society of Chemistry 2022

formation of oxy/hydroxide in the WCoSe/WCo$_3$O$_4$ heterostructure *via* the controlled selenization process could help to solve the constriction of OER electrocatalysts.[4,52]

For further practical applications, the hydrogen evolution reaction (HER) performance of the as-obtained catalysts was investigated by LSV in 1 M KOH electrolyte using a three-electrode setup. Benefiting from optimized heterointerfaces, the WCoSe/WCo$_3$O$_4$ heterostructure electrocatalyst exhibited an excellent HER performance, with a low overpotential of ~98 mV at a current density of 10 mA cm^{-2} (Fig. 4d), which is better than controlled materials (Fig. S10a†) and comparable to the commercial Pt/C catalyst on NF (~77 mV). The outstanding catalytic properties of the WCoSe/WCo$_3$O$_4$ heterostructure were represented by the required overpotential at current densities of 10 and 100 cm^{-2} (Fig. 4f). Moreover, it shows more excellent characteristics than previously reported electrocatalysts for the HER (Table S2†).[53,54] In addition, the WCoSe/WCo$_3$O$_4$ catalyst exhibits a low Tafel slope of ~72 mV dec^{-1}, which is better than that of the corresponding precursor (Fig. S10b†), CoSe/Co$_3$O$_4$ (~90.5 mV dec^{-1}) and WSe$_2$/WO$_2$ (~110 mV dec^{-1}), and comparable to that of the commercial Pt/C catalyst (~41 mV dec^{-1}), as shown in Fig. 4f, demonstrating that the WCoSe/WCo$_3$O$_4$ heterostructure is promising for maximizing the HER kinetics and suggesting that it follows the typical Volmer–Tafel mechanism and accelerates the H$_2$ formation in alkaline electrolyte.[1,55,56] The intrinsic resistance of all the as-obtained electrocatalysts was characterized by EIS (Fig. S11†). The WCoSe/WCo$_3$O$_4$ heterostructure possesses a lower R_{ct} value of ~0.52 Ω than CoSe/Co$_3$O$_4$ (~0.64 Ω), WSe$_2$/WO$_2$ (~0.76 Ω), and Pt/C-NF (~0.56 Ω), respectively, which enhances the electrochemical HER performance. Moreover, the electroactive sites for the HER were derived by evaluating the double-layer capacitance of the electrocatalysts. The WCoSe/WCo$_3$O$_4$ heterostructure possesses a high C_{dl} value of ~39.2 mF cm^{-2}, which is higher than that of the comparative catalysts of CoSe/Co$_3$O$_4$ (~32.1 mF cm^{-2}) and WSe$_2$/WO$_2$ (~24.6 mF cm^{-2}), representing its exceptional electroactive sites (Fig. S12a–d†). To further confirm the durability of the WCoSe/WCo$_3$O$_4$ heterostructure catalyst, we performed the chronopotentiometric technique with a fixed potential of −0.3 V. The potential response showed a negligible degradation after 50 h. After the stability test, the polarization LSV curves showed a slight shift demonstrating the tremendous electrochemical durability of the WCoSe/WCo$_3$O$_4$ electrocatalyst (Fig. S13†). The EIS after the stability test indicates that the WCoSe/WCo$_3$O$_4$ heterostructure with the lowest R_{ct} value of ~0.58 Ω after the prolonged cycling test suggests its exceptional HER durability. In addition, the SEM image of the WCoSe/WCo$_3$O$_4$ heterostructure electrocatalyst after the stability test exhibited a minimal morphology change without structural damage (Fig. S14†).

Overall water splitting performances

Based on the excellent OER and HER performance, we have assembled the WCoSe/WCo$_3$O$_4$ heterostructure as bifunctional catalysts for overall water splitting devices in 1 M KOH electrolyte. The fabrication and structure of water splitting devices are illustrated in Fig. 5a. Remarkably, the WCoSe/WCo$_3$O$_4$-∥WCoSe/WCo$_3$O$_4$ water electrolyzer required a small voltage of 1.498 V to reach the current density of 10 mA cm^{-2} (Fig. 5b), outperforming the state-of-the-art Pt/C∥RuO$_2$ water-splitting cell, which needs a potential of 1.498 V to reach the current density of 10 mA cm^{-2}, which is superior to those in recently reported literature for overall water splitting electrocatalysts.[57–59] To further examine the long-term stability of the WCoSe/WCo$_3$O$_4$ bifunctional catalyst toward water splitting, we performed the chronopotentiometric test for our WCoSe/WCo$_3$O$_4$∥WCoSe/WCo$_3$O$_4$ electrolyzer at a high current density of 100 mA cm^{-2}. As shown in Fig. 5c, the as-fabricated water splitting devices displayed an excellent durability for 100 h with a slight cell-voltage increase of ~2.5%. In contrast, the cell-voltage of the Pt/C∥RuO$_2$ water splitting device increased by 35.2% after 18 h (Fig. S15†), confirming that our WCoSe/WCo$_3$O$_4$∥WCoSe/WCo$_3$O$_4$ device shows excellent durability and could be applied for practical applications. Notably, we also collected the total quantity of hydrogen (H$_2$) and oxygen (O$_2$) by the water drainage method to measure the faradaic efficiency (Fig. 5d). The volume ratio of the collected hydrogen to oxygen is about 2.05 : 1, approaching the theoretical ratio (2 : 1), displaying its nearly 100% faradaic efficiency for water splitting. To realize the durable nature of the WCoSe/WCo$_3$O$_4$ heterostructure electrocatalyst, the post-treated catalysts were examined by morphological and structural studies. As shown by the SEM and TEM images in Fig. S16,† both the post-OER and post-HER side electrodes in overall water splitting retain their original structure without obvious change, demonstrating their outstanding electrochemical stability. The high-resolution XPS was used to further confirm the stability of the structure. The post-HER and post-OER side electrodes showed small upward shifts for W 4f and Co 2p, while the trivial downshifts observed for O 1s and Se 3d proves that the WCoSe/WCo$_3$O$_4$ heterostructure electrocatalyst has ultra-long term stability during the long-term operation (Fig. S17†). Overall, the results demonstrate that the excellent OER and HER activities are facilitated by the synergetic effect of the selenization/oxidation-induced surface and make them promising candidates for overall water splitting in an alkaline medium.

The superior performance of the 3D hierarchical WCoSe/WCo$_3$O$_4$ heterostructure is analyzed based on the results of the above experiments which could be attributed to the following facts. Firstly, the 3D network structure is advantageous for adequate mass transportation between the electrolyte and electrode and an efficient pathway for rapid charge transport and gas escape from the catalyst surface during the reaction process. Secondly, the constructed heterostructure can facilitate the electron transfer, exhibiting a synergistic effect that enhances the catalyst stability by the selenization/oxidation-induced surface interface strategy and favors fast electron transport in the electrocatalytic process. Finally, the morphology and heterostructure interface in WCoSe/WCo$_3$O$_4$ with strong electron interaction promote the initiation of abundant electroactive sites by interfacial engineering which eventually accelerates the water splitting kinetics. The partial

This journal is © The Royal Society of Chemistry 2022

J. Mater. Chem. A, 2022, **10**, 3782–3792 | **3789**

Fig. 5 Electrocatalytic performance of the water splitting cell in an alkaline medium: (a) illustration of the electrochemical water splitting device, (b) LSV curves of the WCoSe/WCo$_3$O$_4$‖WCoSe/WCo$_3$O$_4$ and Pt/C‖RuO$_2$-NF devices in 1.0 M KOH, (c) long-term stability test of the WCoSe/WCo$_3$O$_4$‖WCoSe/WCo$_3$O$_4$ electrochemical water splitting device at a current density of 100 mA cm^{-2} over 100 h (inset shows the generation of H$_2$ and O$_2$ during the electrocatalytic process), and (d) the setup measurement of H$_2$ and O$_2$ generation during water electrolysis.

oxidation process with enriched oxygen sites could enhance the durability of materials during the OER and water splitting.

Conclusions

In summary, we have engineered a 3D hierarchical WCoSe/WCo$_3$O$_4$ heterostructure by the selenization/oxidation induced surface modification strategy. The extraordinarily enhanced electrocatalytic performance of the 3D hierarchical WCoSe/WCo$_3$O$_4$ heterostructure benefits from the simultaneous modulation of the electronic configuration, large surface area with abundant active sites, abundant heterogeneous interfaces, and exceptional synergistic effect. Moreover, it could boost the bifunctional catalytic activity toward the OER and HER under alkaline conditions. The surface oxidation of bimetallic selenide could enhance the active sites helping to improve the OER performance durability, thereby increasing the cycle life of the water splitting electrolyzer. Benefiting from the excellent OER and HER performance, the assembled WCoSe/WCo$_3$O$_4$‖WCoSe/WCo$_3$O$_4$ electrolyzer can generate current densities of 10 and 100 mA cm^{-2} with low cell voltages of ∼1.49 V and 1.66 V, respectively, with excellent durability. This work reveals the effective fabrication technique and robust electrocatalyst that together promote the electrocatalytic activity for bifunctional water splitting.

Conflicts of interest

There are no conflicts to declare.

Acknowledgements

Notes and references

1 Y. Shi and B. Zhang, *Chem. Soc. Rev.*, 2016, **45**, 1529–1541.
2 X. Qin, D. Kim and Y. Piao, *Carbon Energy*, 2021, **3**, 66–100.

3790 | *J. Mater. Chem. A*, 2022, **10**, 3782–3792

This journal is © The Royal Society of Chemistry 2022

3 T.-Y. Jeon, S.-H. Yu, S. J. Yoo, H.-Y. Park and S.-K. Kim, *Carbon Energy*, 2021, **3**, 375–383.

4 M. Wang, L. Zhang, Y. He and H. Zhu, *J. Mater. Chem. A*, 2021, **9**, 5320–5363.

5 H.-x. Zhong, Q. Zhang, J. Wang, X.-b. Zhang, X.-l. Wei, Z.-j. Wu, K. Li, F.-l. Meng, D. Bao and J.-m. Yan, *ACS Catal.*, 2018, **8**, 3965–3970.

6 J. Bai, N. Jia, P. Jin, P. Chen, J.-X. Jiang, J.-H. Zeng and Y. Chen, *J. Energy Chem.*, 2020, **51**, 105–112.

7 I. Roger, M. A. Shipman and M. D. Symes, *Nat. Rev. Chem.*, 2017, **1**, 1–13.

8 L. An, Z. Zhang, J. Feng, F. Lv, Y. Li, R. Wang, M. Lu, R. B. Gupta, P. Xi and S. Zhang, *J. Am. Chem. Soc.*, 2018, **140**, 17624–17631.

9 S. Gupta, M. K. Patel, A. Miotello and N. Patel, *Adv. Funct. Mater.*, 2020, **30**, 1906481.

10 K. L. Zhou, Z. Wang, C. B. Han, X. Ke, C. Wang, Y. Jin, Q. Zhang, J. Liu, H. Wang and H. Yan, *Nat. Commun.*, 2021, **12**, 1–10.

11 P. Lettenmeier, L. Wang, U. Golla-Schindler, P. Gazdzicki, N. A. Cañas, M. Handl, R. Hiesgen, S. S. Hosseiny, A. S. Gago and K. A. Friedrich, *Angew. Chem.*, 2016, **128**, 752–756.

12 T.-J. Wang, H.-Y. Sun, Q. Xue, M.-J. Zhong, F.-M. Li, X. Tian, P. Chen, S.-B. Yin and Y. Chen, *Sci. Bull.*, 2021, **66**, 2079–2089.

13 Y.-H. Fang and Z.-P. Liu, *J. Am. Chem. Soc.*, 2010, **132**, 18214–18222.

14 H. J. Song, H. Yoon, B. Ju, G. H. Lee and D. W. Kim, *Adv. Energy Mater.*, 2018, **8**, 1802319.

15 E. Hu, Y. Feng, J. Nai, D. Zhao, Y. Hu and X. W. D. Lou, *Energy Environ. Sci.*, 2018, **11**, 872–880.

16 Y. Li, Y. Sun, Y. Qin, W. Zhang, L. Wang, M. Luo, H. Yang and S. Guo, *Adv. Energy Mater.*, 2020, **10**, 1903120.

17 X. Gao, Y. Yu, Q. Liang, Y. Pang, L. Miao, X. Liu, Z. Kou, J. He, S. J. Pennycook and S. Mu, *Appl. Catal., B*, 2020, **270**, 118889.

18 H. Wang, H.-W. Lee, Y. Deng, Z. Lu, P.-C. Hsu, Y. Liu, D. Lin and Y. Cui, *Nat. Commun.*, 2015, **6**, 1–8.

19 M. Kim, J. Park, H. Ju, J. Y. Kim, H.-S. Cho, C.-H. Kim, B.-H. Kim and S. W. Lee, *Energy Environ. Sci.*, 2021, **14**, 3053–3063.

20 G. Zhang, J. Zeng, J. Yin, C. Zuo, P. Wen, H. Chen and Y. Qiu, *Appl. Catal., B*, 2021, **286**, 119902.

21 H. Xu, H. Shang, C. Wang, L. Jin, C. Chen, C. Wang and Y. Du, *Appl. Catal., B*, 2020, **265**, 118605.

22 T. T. Nguyen, J. Balamurugan, K.-T. Lau, N. H. Kim and J. H. Lee, *J. Mater. Chem. A*, 2021, **9**, 9092–9104.

23 P. Du and R. Eisenberg, *Energy Environ. Sci.*, 2012, **5**, 6012–6021.

24 D. Xu, X. Long, J. Xiao, Z. Zhang, G. Liu, H. Tong, Z. Liu, N. Li, D. Qian and J. Li, *Chem. Eng. J.*, 2021, **422**, 129982.

25 X. Peng, Y. Yan, X. Jin, C. Huang, W. Jin, B. Gao and P. K. Chu, *Nano Energy*, 2020, 105234.

26 J. Balamurugan, T. T. Nguyen, D. H. Kim, N. H. Kim and J. H. Lee, *Appl. Catal., B*, 2021, **286**, 119909.

27 Z. Li, K. Wang, X. Tan, X. Liu, G. Wang, G. Xie and L. Jiang, *Chem. Eng. J.*, 2021, **424**, 130390.

28 C. Cai, S. Han, W. Liu, K. Sun, L. Qiao, S. Li and X. Zu, *Appl. Catal., B*, 2020, **260**, 118103.

29 Y. Song, J. Cheng, J. Liu, Q. Ye, X. Gao, J. Lu and Y. Cheng, *Appl. Catal., B*, 2021, **298**, 120488.

30 L. Yang, L. Huang, Y. Yao and L. Jiao, *Appl. Catal., B*, 2021, **282**, 119584.

31 J. Wang, H.-x. Zhong, Y.-l. Qin and X.-b. Zhang, *Angew. Chem., Int. Ed.*, 2013, **52**, 5248–5253.

32 H. Liu, D. Zhao, P. Hu, K. Chen, X. Wu and D. Xue, *Mater. Today Phys.*, 2020, **13**, 100197.

33 F. Song, W. Li, J. Yang, G. Han, P. Liao and Y. Sun, *Nat. Commun.*, 2018, **9**, 4531.

34 L. Yuan, S. Liu, S. Xu, X. Yang, J. Bian, C. Lv, Z. Yu, T. He, Z. Huang, D. W. Boukhvalov, C. Cheng, Y. Huang and C. Zhang, *Nano Energy*, 2021, **82**, 105732.

35 J. Wang, T. Liao, Z. Wei, J. Sun, J. Guo and Z. Sun, *Small Methods*, 2021, **5**, 2000988.

36 D. Liu, H. Ai, M. Chen, P. Zhou, B. Li, D. Liu, X. Du, K. H. Lo, K. W. Ng and S. P. Wang, *Small*, 2021, **17**, 2007557.

37 X. Luo, P. Ji, P. Wang, R. Cheng, D. Chen, C. Lin, J. Zhang, J. He, Z. Shi and N. Li, *Adv. Energy Mater.*, 2020, **10**, 1903891.

38 X. Zheng, X. Han, Y. Cao, Y. Zhang, D. Nordlund, J. Wang, S. Chou, H. Liu, L. Li and C. Zhong, *Adv. Mater.*, 2020, **32**, 2000607.

39 P. Zhai, Y. Zhang, Y. Wu, J. Gao, B. Zhang, S. Cao, Y. Zhang, Z. Li, L. Sun and J. Hou, *Nat. Commun.*, 2020, **11**, 1–12.

40 H. Zhu, J. Zhang, R. Yanzhang, M. Du, Q. Wang, G. Gao, J. Wu, G. Wu, M. Zhang and B. Liu, *Adv. Mater.*, 2015, **27**, 4752–4759.

41 H. Zhong, J. Wang, F. Meng and X. Zhang, *Angew. Chem., Int. Ed.*, 2016, **55**, 9937–9941.

42 S. R. Kadam, A. N. Enyashin, L. Houben, R. Bar-Ziv and M. Bar-Sadan, *J. Mater. Chem. A*, 2020, **8**, 1403–1416.

43 G. Zhang, X. Zheng, Q. Xu, J. Zhang, W. Liu and J. Chen, *J. Mater. Chem. A*, 2018, **6**, 4793–4800.

44 M. Sakthivel, S. Ramki, S.-M. Chen and K.-C. Ho, *Nanoscale*, 2020, **12**, 15752–15766.

45 Z. Lin, B. Xiao, Z. Wang, W. Tao, S. Shen, L. Huang, J. Zhang, F. Meng, Q. Zhang and L. Gu, *Adv. Funct. Mater.*, 2021, 2102321.

46 M. S. Sokolikova, P. C. Sherrell, P. Palczynski, V. L. Bemmer and C. Mattevi, *Nat. Commun.*, 2019, **10**, 1–8.

47 Z. Liang, S. Yang, X. Wang, H. Cui, X. Wang and J. Tian, *Appl. Catal., B*, 2020, **274**, 119114.

48 P. Li, M. Wang, X. Duan, L. Zheng, X. Cheng, Y. Zhang, Y. Kuang, Y. Li, Q. Ma, Z. Feng, W. Liu and X. Sun, *Nat. Commun.*, 2019, **10**, 1711.

49 R. Blume, P. R. Kidambi, B. C. Bayer, R. S. Weatherup, Z.-J. Wang, G. Weinberg, M.-G. Willinger, M. Greiner, S. Hofmann, A. Knop-Gericke and R. Schlögl, *Phys. Chem. Chem. Phys.*, 2014, **16**, 25989–26003.

50 R. Balaji, J. Balamurugan, T. T. Nguyen, N. H. Kim and J. H. Lee, *Chem. Eng. J.*, 2020, **390**, 124557.

51 T. T. Nguyen, J. Balamurugan, D. H. Kim, N. H. Kim and J. H. Lee, *Small*, 2020, **16**, 2004661.

This journal is © The Royal Society of Chemistry 2022

J. Mater. Chem. A, 2022, **10**, 3782–3792 | **3791**

52 J. Zhang, T. Wang, D. Pohl, B. Rellinghaus, R. Dong, S. Liu, X. Zhuang and X. Feng, *Angew. Chem., Int. Ed.*, 2016, **55**, 6702–6707.

53 C. C. Yang, S. F. Zai, Y. T. Zhou, L. Du and Q. Jiang, *Adv. Funct. Mater.*, 2019, **29**, 1901949.

54 J. Diao, Y. Qiu, S. Liu, W. Wang, K. Chen, H. Li, W. Yuan, Y. Qu and X. Guo, *Adv. Mater.*, 2020, **32**, 1905679.

55 J. Huang, J. Han, T. Wu, K. Feng, T. Yao, X. Wang, S. Liu, J. Zhong, Z. Zhang and Y. Zhang, *ACS Energy Lett.*, 2019, **4**, 3002–3010.

56 J. Balamurugan, T. T. Nguyen, N. H. Kim, D. H. Kim and J. H. Lee, *Nano Energy*, 2021, **85**, 105987.

57 H. Wang, Z.-n. Chen, D. Wu, M. Cao, F. Sun, H. Zhang, H. You, W. Zhuang and R. Cao, *J. Am. Chem. Soc.*, 2021, **143**, 4639–4645.

58 H. Guo, A. Wu, Y. Xie, H. Yan, D. Wang, L. Wang and C. Tian, *J. Mater. Chem. A*, 2021, **9**, 8620–8629.

59 L. Chai, Z. Hu, X. Wang, Y. Xu, L. Zhang, T.-T. Li, Y. Hu, J. Qian and S. Huang, *Adv. Sci.*, 2020, **7**, 1903195.